

**NASA Technical Paper 1082**

**Mechanical Behavior  
and Fracture Characteristics  
of Off-Axis Fiber Composites  
II - Theory and Comparisons**

**CASE FILE  
COPY**

**Christos C. Chamis and John H. Sinclair**

**JANUARY 1978**

**NASA**

NASA Technical Paper 1082

**Mechanical Behavior  
and Fracture Characteristics  
of Off-Axis Fiber Composites  
II - Theory and Comparisons**

Christos C. Chamis and John H. Sinclair  
Lewis Research Center  
Cleveland, Ohio

**NASA**

National Aeronautics  
and Space Administration

**Scientific and Technical  
Information Office**

1978

MECHANICAL BEHAVIOR AND FRACTURE CHARACTERISTICS  
OF OFF-AXIS FIBER COMPOSITES  
II - THEORY AND COMPARISONS

by Christos C. Chamis and John H. Sinclair

Lewis Research Center

SUMMARY

A theoretical investigation was conducted to study the mechanical behavior and fracture characteristics of high-modulus graphite-fiber/epoxy unidirectional composites subjected to off-axis tensile load. The results were compared with experimental data. The investigation included the use of composite mechanics, combined-stress failure criteria, and finite-element analysis to analyze off-axis specimens loaded at various angles ( $0^{\circ}$  to  $90^{\circ}$ ) to the fiber direction.

The predicted results, using composite mechanics, were in very good agreement with measured data for modulus, Poisson's ratio, and shear coupling coefficient. The fracture stresses predicted by the modified distortion energy, combined-stress failure criterion were in excellent agreement with measured data.

The results obtained using finite-element analysis methods indicated that the axial strain variation is very sensitive to out-of-plane bending and twisting eccentricities as small as about one ply thick. The in-plane and out-of-plane bending effects should be taken into account in interpreting experimental data.

The results obtained herein coupled with parallel experimental studies described in Part I led to the identification of single-stress predominant fracture modes, to the formulation of criteria for characterizing these fracture modes and to the discovery of three convenient plotting procedures for quantifying them.

The results of this investigation should provide a firm basis for identifying, characterizing, and quantifying fracture modes in off-axis and angleplied laminates.

## INTRODUCTION

Off-axis tensile data for unidirectional composites are of considerable interest to the fiber composite community as discussed in Part I (ref. 1).

The objective of the investigation reported herein was to study the mechanical behavior and fracture characteristics of unidirectional, high-modulus graphite-fiber/epoxy composites subjected to off-axis tensile load. The focus was on identifying fracture modes, on formulating criteria to characterize these modes and their associated fracture surfaces, and on developing convenient plotting techniques to quantify them.

The investigation was both experimental and theoretical. In the experimental part described in Part I, strain gages were used to measure the mechanical response of off-axis specimens tested in tension at various angles ( $0^{\circ}$  to  $90^{\circ}$ ) to the fiber direction. Also, the surface morphology of the fractured specimens were examined in detail by use of a scanning electron microscope (SEM). In the theoretical part, reported herein, composite mechanics was used to predict the elastic properties of the off-axis specimens.

Finite elements, including NASTRAN, were used for the stress analysis and a combined-stress failure criterion was used to predict the fracture stress. The predicted results were subsequently compared with the measured data. Theoretical sensitivity studies were used to help explain anomalies in the experimental data. Sensitivity studies were also used to guide the development of convenient plots for quantifying fracture modes. The results of the experimental investigation are described in Part I (ref. 1). Those for the theoretical investigation and the comparisons are described herein.

## SYMBOLS

A	specimen cross section area
E	modulus of elasticity, type and direction denoted by subscripts
$\epsilon$	fracture strain, type and direction denoted by subscripts
G	shear modulus, type and direction denoted by subscripts
$K_{l12}$	coefficient defined by eq. (5)
MOS	margin of safety defined by eq. (13)
P	fracture load
S	fracture stress, type and direction denoted by subscripts

- $x, y, z$  structural axis right-hand system coordinates ( $x$  along the load direction,  $y$  perpendicular to  $x$  in the laminate plane and  $z$  through the thickness)
- $1, 2, 3$  material or ply axis right-hand system coordinates (1 along the fiber direction, 2 perpendicular to the fiber direction in the ply plane, and 3 through the thickness)
- $\epsilon$  strain, type and direction denoted by subscripts
- $\theta$  load angle (angle between load and fiber directions)
- $\nu$  Poisson's ratio, type and direction denoted by subscripts
- $\sigma$  stress, type and direction denoted by subscripts

Subscripts:

- $c$  composite property
- $l$  ply property
- $s$  shear property
- $T$  tensile property
- $x, y, z$  structural axes coordinate directions
- $1, 2, 3$  material axes coordinate direction

## COMPOSITE MECHANICS

Composite mechanics was used to predict the elastic constants, composite fracture stress and strain, ply fracture stresses and strains, ply margin of safety, and region boundaries of single-failure-mode predominance.

### Elastic Constants

The elastic constants of interest in this investigation are the modulus of elasticity along the load direction  $E_{c_{xx}}$ , the Poisson's ratio  $\nu_{c_{xy}}$ , and the shear coupling coefficient  $\nu_{c_{xs}}$ , which is a measure of the shear deformation induced by the stress along the load, or  $x$  direction. These elastic constants,  $E_{c_{xx}}$ ,  $\nu_{c_{xy}}$ , and  $\nu_{c_{xs}}$ , are expressed in terms of unidirection composite elastic constants using well known transformation equations. The equations, respectively, are

$$\frac{1}{E_{cxx}} = \frac{\cos^4\theta}{E_{\ell 11}} + \frac{\sin^4\theta}{E_{\ell 22}} + \frac{1}{4} \left( \frac{1}{2G_{\ell 12}} - \frac{\nu_{\ell 12}}{E_{\ell 11}} \right) \sin^2 2\theta \quad (1)$$

$$\frac{\nu_{cxy}}{E_{cxx}} = -\frac{1}{4} \left( \frac{1+2\nu_{\ell 12}}{E_{\ell 11}} + \frac{1}{E_{\ell 22}} - \frac{1}{G_{\ell 12}} \right) \sin^2 2\theta + \frac{\nu_{\ell 12}}{E_{\ell 11}} \quad (2)$$

$$\frac{\nu_{cxs}}{E_{cxx}} = \left[ \frac{1 + \nu_{\ell 12}}{E_{\ell 22}} \sin^2\theta - \frac{1 + \nu_{\ell 21}}{E_{\ell 11}} \cos^2\theta + \frac{\cos 2\theta}{2G_{\ell 12}} \right] \sin 2\theta \quad (3)$$

where  $\theta$  defines the angle between fiber and load direction,  $E_{\ell 11}$  denotes the modulus of elasticity along the fiber directions,  $E_{\ell 22}$  is the modulus of elasticity transverse to the fiber direction,  $G_{\ell 12}$  is the in-plane (intralaminar) shear modulus, and  $\nu_{\ell 12}$  is the major Poisson's ratio. Note that the subscript  $\ell$  is used to identify the unidirectional property and that the subscripts 1 and 2 denote orthogonal material axes with 1 taken along the fiber direction. Equations (1) to (3) are programmed in the computer code (ref. 2) that was used to predict the elastic constants from the unidirectional composite properties for comparisons with the measured data (from Part I).

The comparison for the modulus  $E_{cxx}$  is shown in figure 1. As can be seen, the comparisons show very good agreement. The comparison for the Poisson's ratio is shown in figure 2. As can be seen, the measured data are below the predicted curve in the load-angle range  $0^\circ < \theta < 45^\circ$ . The agreement is very good at load angles greater than  $45^\circ$ . The comparison for the coupling coefficient  $\nu_{cxs}$  is shown in figure 3. Again, the agreement is very good.

The conclusion to be made from these comparisons is that the predicted curves are in good agreement with the measured data for modulus, Poisson's ratio, and shear coupling coefficients.

The composite fracture stress along the load direction for the various specimens tested was predicted using the following equations:

$$S_{cxx} = \frac{1}{\left[ \frac{\cos^4\theta}{S_{\ell 11T}^2} + \frac{\sin^4\theta}{S_{\ell 22T}^2} + \frac{1}{4} \left( \frac{1}{S_{\ell 12S}^2} - \frac{K_{\ell 12}}{S_{\ell 11T} S_{\ell 22T}} \right) \sin^2 2\theta \right]^{1/2}} \quad (4)$$

$$K_{\ell 12} = K'_{\ell 12} \frac{(1 + 4\nu_{\ell 12} - \nu_{\ell 13})E_{\ell 22} + (1 - \nu_{\ell 23})E_{\ell 11}}{\left[ E_{\ell 11}E_{\ell 22}(2 + \nu_{\ell 12} + \nu_{\ell 13})(2 + \nu_{\ell 21} + \nu_{\ell 23}) \right]^{1/2}} \quad (5)$$

The undefined notation in equations (4) and (5) is as follows:  $K_{\ell 12}$  is a correlation coefficient which is assumed to be unity in this case,  $S_{\ell 11T}$  is the uniaxial longitudinal fracture stress (along the fiber),  $S_{\ell 22T}$  is the uniaxial transverse fracture stress,  $S_{\ell 12S}$  is the uniaxial intralaminar (in-plane) shear fracture stress, and  $\nu_{\ell 13}$  and  $\nu_{\ell 23}$  represent Poisson's ratio in the 3 direction, which is through the composite thickness. The Poisson's ratio  $\nu_{\ell 13}$  is usually taken equal to  $\nu_{\ell 12}$ , and  $\nu_{\ell 23}$  is computed using composite micromechanics. The value of  $K_{\ell 12}$  for the high-modulus, graphite-fiber/epoxy (Mod I/E) composite as computed by the computer code (ref. 2) is 1.44. Note that equations (4) and (5) are derivable from a modified distortion energy principle described in reference 3.

The composite fracture strains  $\mathcal{E}_c$  coinciding with the load direction for the various specimens tested were predicted using the following equations:

$$\mathcal{E}_{cxx} = \frac{S_{cxx}}{E_{cxx}} \quad (6)$$

$$\mathcal{E}_{cyy} = \nu_{cxy} \frac{S_{cxx}}{E_{cxx}} \quad (7)$$

$$\mathcal{E}_{cxy} = \nu_{cxs} \frac{S_{cxx}}{E_{cxx}} \quad (8)$$

where  $S_{cxx}$  is given by  $P/A$  (where  $P$  is the fracture load and  $A$  the specimen cross section area) and the elastic constants are determined using equations (1) to (3).

Equations (4) to (8) have been programmed in the computer code (ref. 2), and the predicted results used for the comparisons were generated using this code.

The comparison for the fracture stress is shown in figure 4. The unidirectional composite fracture stresses (rounded off from table I, ref. 1) used to generate the predicted data are also shown in this figure. As can be seen the comparison is excellent. The comparison for the center gage fracture strains are summarized in table I. The comparison is very good for the axial  $\mathcal{E}_{cxx}$  and shear  $\mathcal{E}_{cxy}$  strains, and it is reasonably good for the Poisson's  $\mathcal{E}_{cyy}$  strain. This good agreement is to be expected when the stress-strain curves are linear (or nearly so) to fracture.

The important conclusion from these comparisons is that the off-axis failure of composites with linear stress-strain curves to fracture is predicted accurately by the failure theory summarized herein and described in detail in reference 3.

## Ply Fracture Stresses and Strains and Ply Margin of Safety

The ply fracture stresses were determined using the following equations:

$$\sigma_{\ell 11} = S_{\text{cxx}} \cos^2 \theta \quad (9)$$

$$\sigma_{\ell 22} = S_{\text{cxx}} \sin^2 \theta \quad (10)$$

$$\sigma_{\ell 12} = \frac{1}{2} S_{\text{cxy}} \sin 2\theta \quad (11)$$

where  $\sigma_{\ell}$  represents ply stress and the numerical subscripts the directions.

The ply fracture strains  $\varepsilon_{\ell}$  were determined using the following matrix equation:

$$\begin{Bmatrix} \varepsilon_{\ell 11} \\ \varepsilon_{\ell 22} \\ \varepsilon_{\ell 12} \end{Bmatrix} = \begin{bmatrix} \cos^2 \theta & \sin^2 \theta & \frac{1}{2} \sin 2\theta \\ \sin^2 \theta & \cos^2 \theta - \frac{1}{2} \sin 2\theta \\ -\sin 2\theta & \sin 2\theta & \cos 2\theta \end{bmatrix} \begin{Bmatrix} \varepsilon_{\text{cxx}} \\ \varepsilon_{\text{cyy}} \\ \varepsilon_{\text{cxy}} \end{Bmatrix} \quad (12)$$

where  $\varepsilon_{\text{c}}$  are the composite strains at fracture which are determined from equations (6) to (8). Equations (9) to (12) are available in the computer code (ref. 2). The predicted results reported herein were generated using this code.

The ply margin of safety (MOS) at fracture, as used herein, was determined using the following equation:

$$\text{MOS} = 1 - \left[ \left( \frac{\sigma_{\ell 11}}{S_{\ell 11T}} \right)^2 + \left( \frac{\sigma_{\ell 22}}{S_{\ell 22T}} \right)^2 + \left( \frac{\sigma_{\ell 12}}{S_{\ell 12S}} \right)^2 - K_{\ell 12} K'_{\ell 12} \frac{\sigma_{\ell 11} \sigma_{\ell 22}}{S_{\ell 11T} S_{\ell 22T}} \right] \quad (13)$$

with the following interpretations:

MOS > 0 no fracture.

MOS = 0 incipient fracture.

MOS < 0 fracture has occurred.

where  $\sigma_{\ell}$  denotes ply stress as determined from equations (9) to (11),  $S_{\ell}$  denotes uniaxial fracture stress,  $K_{\ell 12} = 1.44$ , and  $K'_{\ell 12} = 1.0$ . Note that equation (13), as was equation (4), is derived from the same distortion-energy principle mentioned previously and is available in the computer code (ref. 2). The theoretical predictions reported herein were generated using this code.

Predicted ply fracture strains are summarized in table II. The points to be observed from this table are

(1) The ply fracture shear (intralaminar shear) strains dominates in the load angle range  $5^{\circ} \leq \theta \leq 30^{\circ}$ .

(2) The ply fracture transverse strains dominate in the load angle region  $60^{\circ} < \theta < 90^{\circ}$ .

Predicted ply fracture stresses and margins-of-safety are summarized in table III. Examination of the MOS column reveals that only specimen A-5 has  $MOS > 0$ . This indicates that this specimen did not reach its predicted failure stress according to the failure criterion (eq. (13)). A direct implication from this result is that the specimen failed prematurely and that the test should have been repeated. For example, equation (13) with  $MOS = 0$  predicts a stress of about  $45 \times 10^3$  newtons per square centimeter (65 ksi) at fracture, which is approximately 17 percent higher than measured.

It is clear from this discussion that equation (13) may be used to assess the accuracy of test data in off-axis composite testing. Stated differently, equation (13) may be used as an accept/reject criterion for test data.

#### Regions of Single-Failure Mode Predominance

The regions where single failure modes predominate may be identified by plotting the following ratios from measured data:  $\sigma_{\ell 11}/S_{\ell 11T}$ ,  $\sigma_{\ell 22}/S_{\ell 22T}$ ,  $\sigma_{\ell 12}/S_{\ell 12S}$ ,  $\epsilon_{\ell 11}/\mathcal{E}_{\ell 11T}$ ,  $\epsilon_{\ell 22}/\mathcal{E}_{\ell 22T}$ , and  $\epsilon_{\ell 12}/\mathcal{E}_{\ell 12S}$  as functions of load angle  $\theta$ . In these ratios  $\sigma_{\ell}$  and  $\epsilon_{\ell}$  denote ply stress and strain, respectively, and  $S_{\ell}$  and  $\mathcal{E}_{\ell}$  represent the corresponding uniaxial fracture stress and strain, respectively. Regions of single-failure-mode predominance show only one of these ratios ( $\sigma_{\ell}/S_{\ell}$ ) and ( $\epsilon_{\ell}/\mathcal{E}_{\ell}$ ) near unity, while the other two are considerably smaller by comparison.

The resulting plot for stress is shown in figure 5. As can be observed from this figure, the curve for  $\sigma_{\ell 11}/S_{\ell 11}$  is closer to unity than  $\sigma_{\ell 22}/S_{\ell 22}$  or  $\sigma_{\ell 12}/S_{\ell 12}$ , as observed from the crossover points, in the load-angle range  $0^{\circ} \leq \theta < 5^{\circ}$ ; therefore, longitudinal tension is the predominant fracture mode in this range. The ratio  $\sigma_{\ell 12}/S_{\ell 12}$  is closer to unity as observed from the crossover points in the range  $5^{\circ} < \theta \leq 20^{\circ}$ , indicating that intralaminar shear stress is the predominant fracture mode in this range. The ratio  $\sigma_{\ell 22}/S_{\ell 22}$  is closer to unity as observed from the crossover points in the range  $45^{\circ} \leq \theta \leq 90^{\circ}$  indicating that the transverse tensile stress is the predominant fracture mode in this range. It is important to note that the SEM results in Part I show fracture surface characteristics that are distinctly different in several load angle ranges. The ratios  $\sigma_{\ell 12}/S_{\ell 12S}$  and  $\sigma_{\ell 22}/S_{\ell 22T}$  have comparable magnitudes in the load angle range  $20^{\circ} < \theta < 45^{\circ}$ . In this range, then, fracture is produced by combinations of intralaminar shear and transverse tensile stresses (mixed mode). The fracture surface

in this range will be characterized by mixtures of matrix lacerations, matrix cleavage, and fiber surface free of matrix residue.

The corresponding plot for strains is shown in figure 6. As can be observed in this figure the ratios for strains near unity are the same as those for the corresponding stresses. The load angle in which the individual strains dominate are longitudinal tension  $0^\circ \leq \theta < 5^\circ$ , intralaminar shear  $5^\circ < \theta \leq 20^\circ$ , transverse tension  $45^\circ \leq \theta \leq 90^\circ$ , and mixed mode (combinations of intralaminar shear and transverse tensile)  $20^\circ < \theta < 45^\circ$ .

The "near 0" very narrow load angle range (about  $5^\circ$ ) dominance of longitudinal tensile fracture stress is well known in the fiber composite community. However, the narrow range (about  $15^\circ$ ) of intralaminar shear stress fracture dominance and the large range (about  $60^\circ$ ) of transverse tensile stress fracture stress dominance have not been identified or, at least, not reported previously.

It is important to note at this juncture that the results of figures 5 and 6 provided the theoretical basis for using the  $10^\circ$  off-axis tensile test method for intralaminar shear characterization (ref. 4). This test method was a spinoff of the present investigation.

The major conclusion from this discussion is that the regions of single-stress-fracture-mode dominance are identified by normalized plots of stress and strain. And, furthermore, in these regions the fracture surface SEM photomicrographs (Part I) show distinct fracture mode characteristics, that is, fiber tensile fracture  $0^\circ \leq \theta \leq 5^\circ$ , matrix lacerations  $5^\circ < \theta \leq 20^\circ$ , mixed modes  $20^\circ < \theta < 45^\circ$  and matrix cleavage  $45^\circ \leq \theta \leq 90^\circ$ .

### Stress-Type Influence on Fracture Mode

A procedure to identify regions of individual stress influence on fracture mode is obtained by normalizing the ply stresses with respect to fracture stress in the load direction in equations (9) to (11). As can be seen from these equations the normalization leads to the following trigonometric functions:  $\cos^2\theta$  for longitudinal stress,  $\sin^2\theta$  for transverse stress, and  $(\sin 2\theta)/2$  for intralaminar shear stress. The next step is to plot these functions versus load angle and superimpose the corresponding measured data. The ranges of single-stress-fracture-mode predominance are then identified by the coincidence of the measured data with the corresponding trigonometric function.

This procedure is illustrated graphically in figure 7. The following are observed in figure 7:

(1) The intralaminar shear stress coincides with its corresponding trigonometric function in the load-angle range  $0 < \theta \leq 20^\circ$  and, therefore, has significant influence in this range.

(2) The transverse stress coincides with its corresponding trigonometric function throughout the range of the load angle. It, therefore, influences the fracture mode throughout the range and predominates in the  $30^{\circ} < \theta \leq 90^{\circ}$  range.

(3) The longitudinal stress coincides with its corresponding trigonometric function only at the  $0^{\circ}$  load angle. It, therefore, has insignificant influence in the fracture mode in the  $0^{\circ} < \theta \leq 90^{\circ}$  range.

The conclusion here is that the ranges of individual stress influence and/or pre-dominance on fracture mode are identified by means of the procedure illustrated in figure 7. The results just described coupled with the results of the scanning electron microscope studies (see Part I) should provide a firm basis for identifying, characterizing, and quantifying fracture modes in off-axis and angle-ply laminates.

### Indirect Determination of Intralaminar Fracture Shear Stress

The intralaminar shear fracture stress may be approximated indirectly from off-axis tensile data using the following procedure. Use equation (4) with known values for  $S_{\ell 11T}$  and  $S_{\ell 22T}$  to generate curves for composite fracture stress  $S_{cXX}$  with assumed values of  $S_{\ell 12S}$  and different load angles  $\theta$ . Superimpose on these curves the measured values for  $S_{cXX}$ .

The procedure is illustrated graphically in figure 8. The intralaminar shear stress is then determined by drawing a best-fit (by eye) vertical line of the measured data (dashed line). The intralaminar shear fracture stress, or strength, is the intersection of this vertical line with the abscissa. For the Mod I/E this value is  $5.5 \times 10^3$  newtons per square centimeter ( $N/cm^2$ ; 8 ksi), which is very close to that of the  $10^{\circ}$  off-axis tensile specimen and is within the range of available data in the literature ( $5.2 \times 10^3$  to  $6.2 \times 10^3 N/cm^2$  (7.5 to 9.0 ksi, ref. 3).

The procedure should be equally applicable for the indirect determination of any of the ply uniaxial fracture stresses.

### FINITE-ELEMENT ANALYSIS

Finite-element analyses were performed to investigate theoretically the effects of in-plane and out-of-plane bending, or twisting, and thickness nonuniformity on the axial stress and strain variations across the width of the specimen.

## In-Plane Bending Effects

Off-axis tensile specimens will tend to undergo in-plane bending. This is caused by the coupling between normal and shear deformations: this coupling will tend to deform the specimen in shear. However, the grips prevent the specimen ends from shearing, thereby inducing in-plane bending. This in-plane bending induces axial stress and strain variations across the specimen width. These variations are determined theoretically herein using finite-element analysis.

The finite element used in the analysis is a second-order triangular-plate finite element with six nodes and two displacement degrees of freedom per node. A schematic of the finite-element representation is shown in figure 9. The dimensions used in the analysis were those of the actual test specimens. Those shown in the schematic are for the  $10^0$  off-axis test specimen. Note that the finite-element representation includes the tapered end-tab portions projecting beyond the grip ends. Note also that the finite-element representation consists of 288 elements, 657 nodes, and 1314 degrees of freedom.

Finite-element analysis results for the axial stress variation, near the end tab (node line 73 to 81, fig. 9) are summarized graphically in figure 10. These stress variations were determined using the fracture load of the specimen and the elastic constants summarized in table IV. As can be seen in figure 10, the most significant axial stress variation is for the  $10^0$  off-axis specimen with a maximum difference of  $16.6 \times 10^3$  N/cm<sup>2</sup> (24 ksi) from edge-to-edge ( $46 \times 10^3$  to  $30 \times 10^3$  N/cm<sup>2</sup> (67 to 43 ksi)). Additional discussion on this variation is given in reference 4. The next axial stress significant variation is that for the  $15^0$  off-axis specimen with a maximum difference of  $7.8 \times 10^3$  N/cm<sup>2</sup> (13 ksi) from edge-to-edge ( $26 \times 10^3$  to  $17 \times 10^3$  N/cm<sup>2</sup> (38 to 25 ksi)). The axial stress variation for the remaining specimens is relatively mild and may be considered as insignificant. An interesting result in figure 10 is the stress reversal trend from  $5^0$  (increasing left to right) to  $10^0$  (decreasing).

The important observation from the preceding discussion is that off-axis tensile specimens show high axial stresses at the edges near the grips in the  $5^0$  to  $15^0$  load angle range and, consequently, fracture should initiate in this region. This, however, is not in agreement with the fracture surfaces shown in figure 14 of Part I, which lead to the suspicion that out-of-plane bending and/or twisting occurred during testing.

Corresponding results for the axial strain variation are shown in figure 11. Here, again, the significant axial strain variation across the specimen width is for the  $10^0$  and  $15^0$  off-axis specimens. These results illustrate the importance of placing strain gages as close to the edge as possible near the end-tab region.

Finite-element results for the axial stress variation at the specimen midlength (center) are shown in figure 12. Only the  $10^0$  off-axis specimen shows a significant variation (about  $9 \times 10^3$  N/cm<sup>2</sup> (13 ksi)) from edge-to-edge ( $39 \times 10^3$  N/cm<sup>2</sup> to  $30 \times 10^3$

N/cm<sup>2</sup> (56 to 43 ksi)). Corresponding results for axial strain are shown in figure 13. As can be seen in this figure, only the 10<sup>0</sup> and 15<sup>0</sup> off-axis specimens show significant variations from edge-to-edge.

The important observation here is that in-plane bending produces significant axial stress variation at midlength only in the 10<sup>0</sup> off-axis specimen. The significance of this observation is that the P/A (fracture load/cross section area) stress is a very good approximation to the actual axial stress at the center of the off-axis specimens. And, in addition, the fracture stress determined from P/A would probably be on the conservative side. It is important to keep in mind that these comments apply to specimens with the gage length-to-width ratios tested herein, which were 14 or greater.

Comparison of finite-element predicted axial strains with measured data near the specimen end tab at fracture load are shown in figure 14. Corresponding results at the specimen midlength are shown in figure 15. As can be seen from these figures, the agreement is reasonably good for the three specimens near the end tab and the 60<sup>0</sup> specimen at midlength. However, the agreement for the 10<sup>0</sup> and 30<sup>0</sup> specimens at midlength is relatively poor. The predicted results are about 10 to 20 percent higher than the measured data at the left edge and center and are less than 10 percent at the right edge.

Some factors that may have contributed to this poor agreement between predicted and measured fracture strains at midlength of the 10<sup>0</sup> and 30<sup>0</sup> off-axis specimens are

- (1) Inability to simulate mathematically exactly the physical boundary conditions
- (2) Nonlinear material behavior near fracture
- (3) Out-of-plane eccentricities - bending and/or twisting
- (4) Variation in specimen thickness.

Item (1) was extensively studied via sensitivity analysis in reference 4 and found to have an effect of less than 5 percent. Item (2) is not believed to have any significant contribution because the stress strain curves (figs. 6 and 8, Part I) are linear to fracture. Items (3) and (4) were investigated herein and are described in the next section. Note that item (3) was also discussed in reference 5.

### Out-of-Plane Bending and Twisting Effects

The effects of out-of-plane bending and twisting on axial strain were evaluated for the 10<sup>0</sup> and 30<sup>0</sup> off-axis specimens using NASTRAN (NASA Structural Analysis Finite Element computer program, ref. 6). The NASTRAN model of the specimen is shown in figure 16. The NASTRAN model consisted of 657 nodes (1971 degrees of freedom) and 576 quadrilateral plate bending elements, which included the tapered portion of the reinforcing end tabs. Note that the finite-element representation includes two groups of elements. At each end the elements are 0.159 centimeter (0.0625 in.) long; these re-

present the tapered portion of the reinforcing tabs and the first quarter inch segment of the test section, which is the site of the top strain gages. The remaining elements of the representation are 0.318 centimeter (0.125 in.) long. All elements for this model are 0.159 centimeter (0.0625 in.) wide. The element size was made small enough to study the zones where the strain gages were located on the actual specimen. The material properties required for NASTRAN were generated from the elastic constants in table IV. The load for both the out-of-plane bending and twisting moments was 11.3 newton-meters (100 in.-lb). The value of 11.3 newton-meters (100 in. lb) was selected mainly for convenience. It corresponds roughly to an eccentricity of a laminate thickness. The effects of smaller eccentricities are readily obtained by direct proportion since a linear stress analysis was performed.

NASTRAN undeformed and deformed plots due to out-of-plane bending moments are shown in figure 17 for the  $10^{\circ}$  off-axis specimen and in figure 18 for the  $30^{\circ}$  off-axis specimen. As can be seen in these plots the deformation for both bending and twisting are considerable.

The axial strain variation due to bending moments across the specimen width predicted using NASTRAN is shown in figure 19 (solid lines for the  $10^{\circ}$  and interrupted lines for the  $30^{\circ}$  off-axis specimens). Corresponding results for axial strain variation at midlength are shown in figure 20. The curves in these figures show that the axial strain variation can be significant near the grips for both bending and twisting and at midlength for bending. This would tend to explain the differences between predicted and measured data shown in figures 14 and 15 and discussed previously.

Thus we see that out-of-plane eccentricities can contribute significantly to the axial strains. Therefore, care should be taken to keep them to an absolute minimum during testing of off-axis specimens.

The following guidelines may be helpful in instrumenting specimens to detect the presence of out-of-plane eccentricities during testing:

- (1) For out-of-plane bending, place strain gages back-to-back at the specimen edge (fig. 21).

- (2) For out-of-plane twisting, place strain gages at both edges on the same surface of the specimen near the end tab (fig. 21).

- (3) If, during testing, the differences in the readings from the pair of strain gages in (1) or (2) or both become excessively high (say, more than 15 percent), then stop the test and realine the specimen to minimize the out-of-plane eccentricities. The strains already recorded can be used to guide the direction of the realignment.

## Thickness Variation Effects

The effects of specimen thickness variations on the axial strain were investigated using NASTRAN and actual measured thickness variations of the specimen (0.15 to 0.14 cm (0.059 to 0.055 in.)). The finite-element model used is shown in figure 16 and has already been described. The results obtained for the 5° off-axis specimen are compared with those for uniform thickness in figure 22. As can be observed from the curves in this figure the thickness variation effects are negligible.

### SUMMARY OF RESULTS AND CONCLUSIONS

The major results of a theoretical investigation into the mechanical behavior and the stresses inducing fracture of fiber composites subjected to off-axis tensile loadings are

1. The composite mechanics predicted results were in very good agreement with measured data for modulus, Poisson's ratios, and shear coupling coefficient.
2. Composite fracture stresses predicted using the modified distortion energy criterion were in excellent agreement with measured data.
3. A convenient plotting procedure was identified that can be used to identify the single-stress influence on off-axis tensile fracture and thereby assist in identifying predominant fracture modes.
4. The predominant fracture modes and associated load-angle ranges of off-axis tensile specimens were identified as follows:
  - a. Longitudinal tensile (fiber breaks) near 0° load angle
  - b. Intralaminar shear (matrix shear fracture) in the 5° to 20° load-angle range
  - c. Transverse tensile (matrix tensile fracture) in the 45° to 90° load angle range
  - d. Mixed mode (intralaminar shear and transverse tensile) in the 20° to 45° load angle range
5. The intralaminar fracture shear stress was determined to be  $5.5 \times 10^3 \text{ N/cm}^2$  (8 ksi) using an indirect plotting procedure developed during this investigation. This value is in good agreement with literature values  $5.2$  to  $6.2 \times 10^3 \text{ N/cm}^2$  (7.5 to 9.0 ksi).
6. The second-order triangular finite-element predicted results showed that in-plane bending has considerable influence in the axial strain variation across the width of the specimen. This influence is most significant in the 5° to 30° load-angle range. The predicted fracture strain variation was off by about 20 percent from the measured data.
7. NASTRAN predicted results showed that thickness variations in the specimen (0.14 to 0.15 cm (0.055 to 0.059 in.)) have negligible effect on the axial strain variation across the specimen width.

8. NASTRAN predicted results showed that out-of-plane bending and twisting eccentricities have significant effects on the axial strain variation across the width for specimens in the  $10^{\circ}$  to  $30^{\circ}$  load-angle range.

9. Care should be taken to minimize eccentricities that will induce out-of-plane bending and twisting since these eccentricities have significant effect on the axial strain.

10. Fracture stress of off-axis tensile specimens determined by load to area ratio should be on the conservative side.

11. The results of this investigation together with the experimental results described in Part I should provide a good foundation for identifying, characterizing, and quantifying fracture modes in off-axis and angleplied laminates.

Lewis Research Center,  
National Aeronautics and Space Administration,  
Cleveland, Ohio, August 25, 1977,  
506-17.

#### REFERENCES

1. Sinclair, John H.; and Chamis, Christos C.: Mechanical Behavior and Fracture Characteristics of Off-Axis Fiber Composites. I - Experimental Investigation. NASA TP-1081, 1977.
2. Chamis, Christos C.: Computer Code for the Analysis of Multilayered Fiber Composites - Users Manual. NASA TN D-7013, 1971.
3. Chamis, Christos C.: Failure Criteria for Filamentary Composites. NASA TN D-5367, 1969.
4. Chamis, Christos C.; and Sinclair, John H.:  $10^{\circ}$  Off-Axis Tensile Test for Intra-laminar Shear Characterization of Fiber Composites. NASA TN D-8215, 1976.
5. Chamis, C. C.; Sinclair, J. H.; and Sullivan, T. L.: NASTRAN as an Analytical Research Tool for Composite Mechanics and Composite Structures. NASA TM X-3428, 1976, pp. 381-417.
6. McCormick, Caleb W., ed.: NASTRAN User's Manual (Level 15). NASA SP-222 (01), 1972.

TABLE I. - COMPARISON OF PREDICTED AND MEASURED  
 FRACTURE STRAINS FOR MOD I/E UNIDIRECTIONAL  
 COMPOSITE TESTED AT VARIOUS ANGLES TO  
 THE FIBER DIRECTION  
 [0.50 Fiber volume fraction]

Specimen	Load angle, deg	Fracture strains, percent,					
		Measured <sup>a</sup>			Predicted		
		Axial, $\epsilon_{cxx}$	Poisson's, $\epsilon_{cyy}$	Shear, $\epsilon_{cxy}$	Axial, $\epsilon_{cxx}$	Poisson's, $\epsilon_{cyy}$	Shear, $\epsilon_{cxy}$
A-0	0	0.231	-0.063	0.0025	0.269	-0.070	0
A-5	5	.188	-.047	.523	.234	-.062	.599
A-10	10	.287	-.046	.985	.351	-.093	1.05
A-15	15	.284	-.057	.743	.331	-.086	.868
A-30	30	.365	-.072	.522	.413	-.093	.596
A-45	45	.390	-.074	.319	.431	-.071	.341
A-60	60	.414	-.030	.152	.445	-.042	.182
A-75	75	.385	-.018	.081	.407	-.014	.069
A-90	90	.364	-.005	.004	.377	-.003	0

<sup>a</sup> $\epsilon_c$  from center gage.

TABLE II. - PREDICTED PLY FRACTURE STRAINS  
 FOR MOD I/E UNIDIRECTIONAL COMPOSITE  
 AS A FUNCTION OF LOAD ANGLE

Specimen	Load angle, deg	Composite fracture strain, <sup>a</sup> percent	Ply strains, percent		
			$\epsilon_{l11}$	$\epsilon_{l22}$	$\epsilon_{l12}$
A-0	0	0.231	0.269	-0.0698	0
A-5	5	.188	.180	-.007	.642
A-10	10	.287	.158	.100	1.14
A-15	15	.284	.0864	.159	.961
A-30	30	.365	.0286	.291	.736
A-45	45	.390	.00913	.351	.502
A-60	60	.414	.00102	.402	.330
A-75	75	.385	-.0026	.396	.151
A-90	90	.364	-.0034	.377	0

<sup>a</sup> $\epsilon_{cxx}$ , center gage, experimental results.

TABLE III. - PREDICTED PLY FRACTURE STRESSES FOR MOD I/E UNIDIRECTIONAL COMPOSITE TESTED AT VARIOUS ANGLES TO THE FIBER DIRECTION

Specimen	Load angle, deg	Experimental composite fracture stress, $S_{c_{xx}}$		Ply stresses						Margin of safety, MOS
				Axial, $\sigma_{l11}$		Transverse, $\sigma_{l22}$		Shear, $\sigma_{l12}$		
				N/cm <sup>2</sup>	ksi	N/cm <sup>2</sup>	ksi	N/cm <sup>2</sup>	ksi	
A-0	0	56.3×10 <sup>3</sup>	81.7	56.3×10 <sup>3</sup>	81.7	0	0	0	0	0.0074
A-5	5	38.1	55.2	37.8	54.8	.3	.4	3.3×10 <sup>3</sup>	4.8	.285
A-10	10	34.3	49.8	33.3	48.3	1.0×10 <sup>3</sup>	1.5	5.9	8.5	.302
A-15	15	19.8	28.7	18.5	26.8	1.3	1.9	5.0	7.2	.0840
A-30	30	8.7	12.6	6.6	9.5	2.2	3.2	3.8	5.5	.0166
A-45	45	5.2	7.5	2.6	3.8	2.6	3.8	2.6	3.8	.0390
A-60	60	3.9	5.7	.97	1.4	3.0	4.3	1.7	2.5	.211
A-75	75	3.1	4.5	.21	.3	2.9	4.2	.8	1.1	.116
A-90	90	2.8	4.0	0	0	2.8	4.0	0	0	0

TABLE IV. - PREDICTED COMPOSITE ELASTIC CONSTANTS - STRUCTURAL AXES FOR MOD I/E

[Used in finite-element analyses.]

Specimen	Load angle, deg	Composite elastic constants								
		Moduli						Poisson's ratio, $\nu_{cxy}$	Coupling coefficients	
		$E_{c_{xx}}$		$E_{c_{yy}}$		$E_{c_{xy}}$				
		N/cm <sup>2</sup>	psi	N/cm <sup>2</sup>	psi	N/cm <sup>2</sup>	psi		$\nu_{cxs}$	$\nu_{cys}$
A-0	0	21.0×10 <sup>6</sup>	30.4×10 <sup>6</sup>	0.73×10 <sup>6</sup>	1.06×10 <sup>6</sup>	0.515×10 <sup>6</sup>	0.747×10 <sup>6</sup>	0.260	0	0
A-5	5	16.3	23.6	.73	1.06	.519	.753	.263	2.56	.053
A-10	10	9.79	14.2	.74	1.08	.531	.770	.265	3.00	.109
A-15	15	5.97	8.66	.77	1.11	.550	.798	.261	2.62	.170
A-30	30	2.12	3.07	.88	1.28	.638	.926	.225	1.44	.410
A-45	45	1.20	1.74	1.20	1.74	.696	1.01	.165	.793	.793
A-60	60	.88	1.28	2.12	3.07	.638	.926	.094	.410	1.44
A-75	75	.77	1.11	5.97	8.66	.550	.798	.033	.170	2.62
A-90	90	.73	1.06	21.0	30.4	.515	.747	.009	0	0

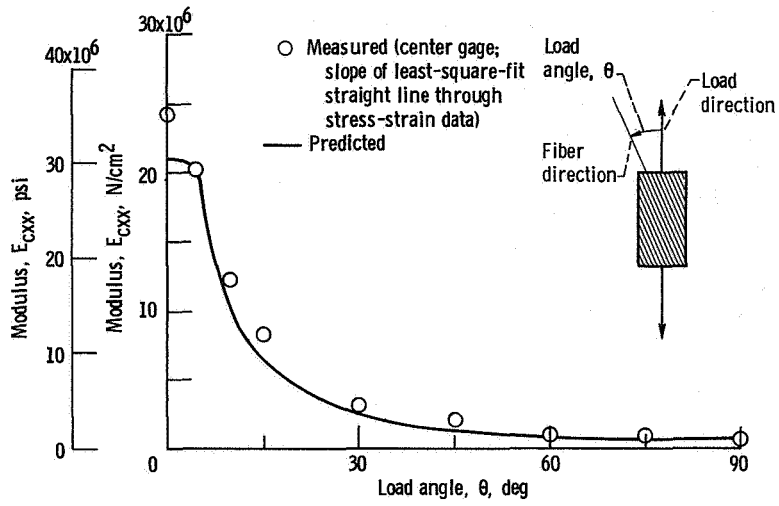


Figure 1. - Modulus for Mod I/E unidirectional composite tested at various angles to fiber direction.

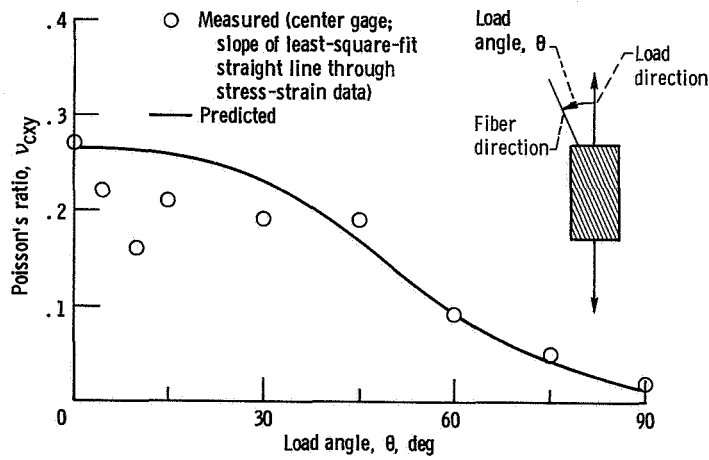


Figure 2. - Poisson's ratio for Mod I/E unidirectional composite tested at various angles to fiber direction.

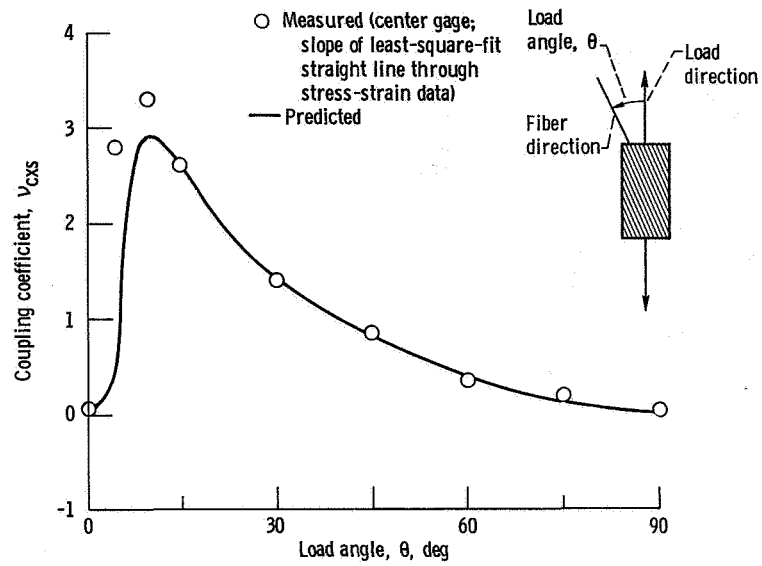


Figure 3. - Coupling coefficient for Mod I/E unidirectional composite tested at various angles to fiber direction.

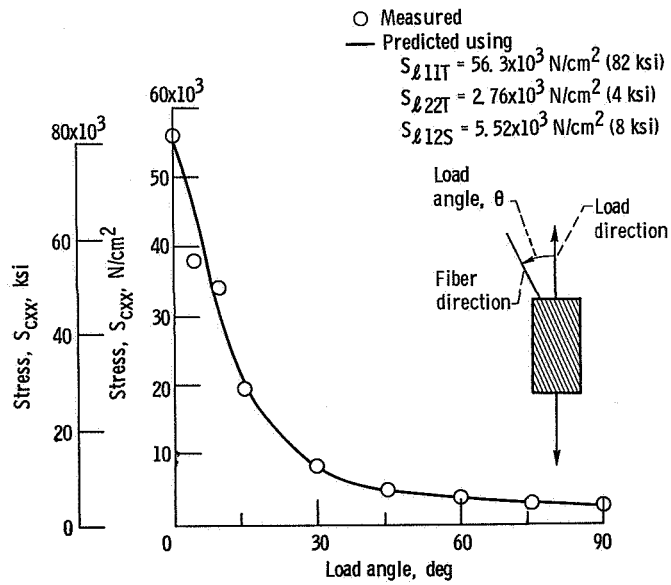


Figure 4. - Comparison of predicted and measured fracture stresses at various test angles for Mod I/E unidirectional composite.

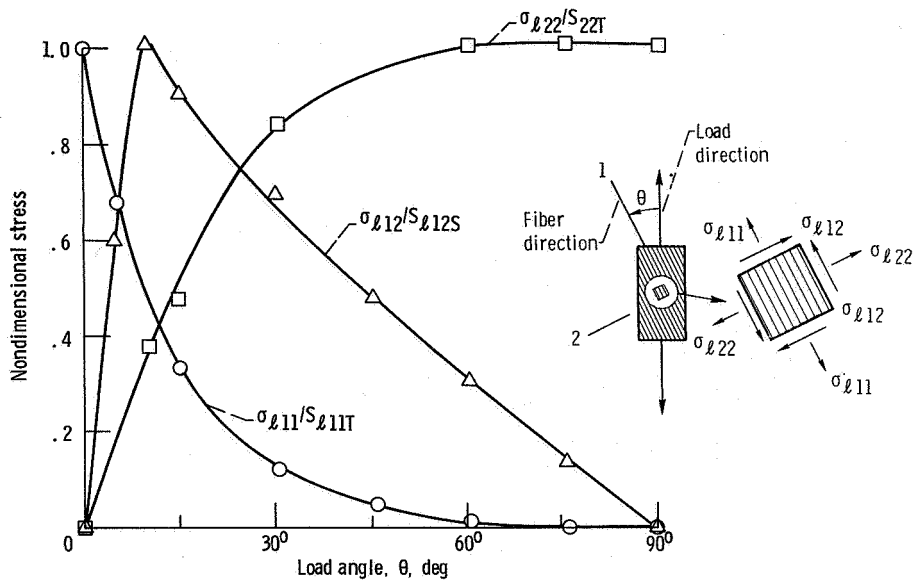


Figure 5. - Fracture stresses normalized with their respective uniaxial strengths ( $S_{\ell}$ ).

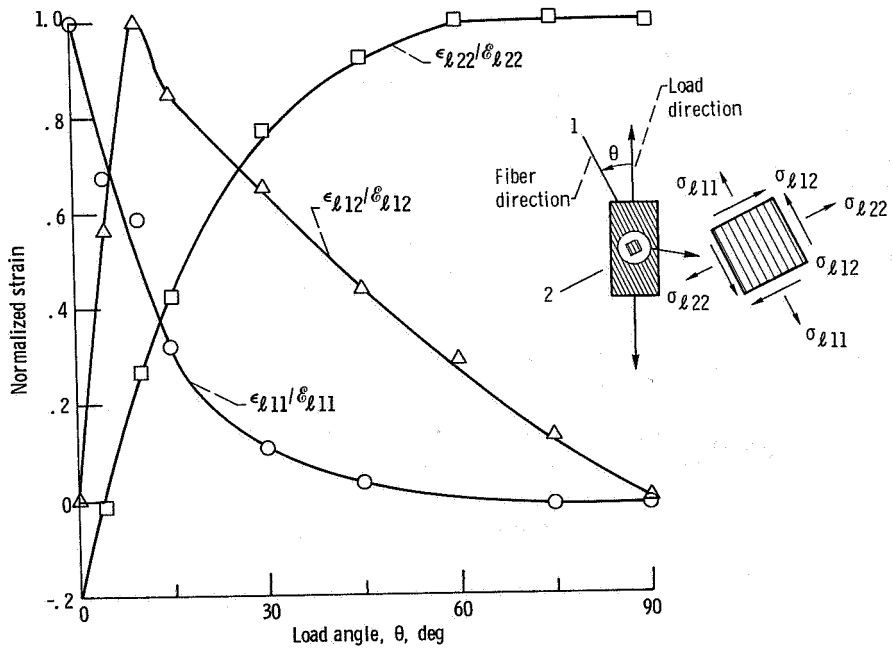


Figure 6. - Ply fracture strains normalized with their respective uniaxial fracture strains (Mod I/E).

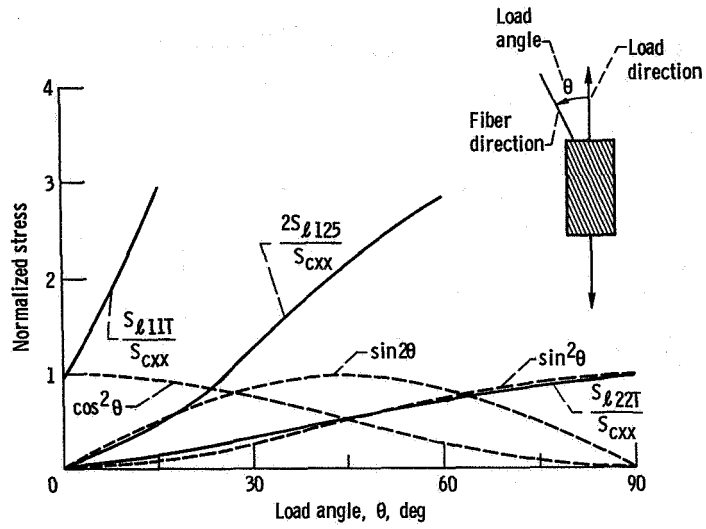


Figure 7. - Ply fracture stresses normalized with respect to specimen fracture stresses at various test angles (Mod I/E).

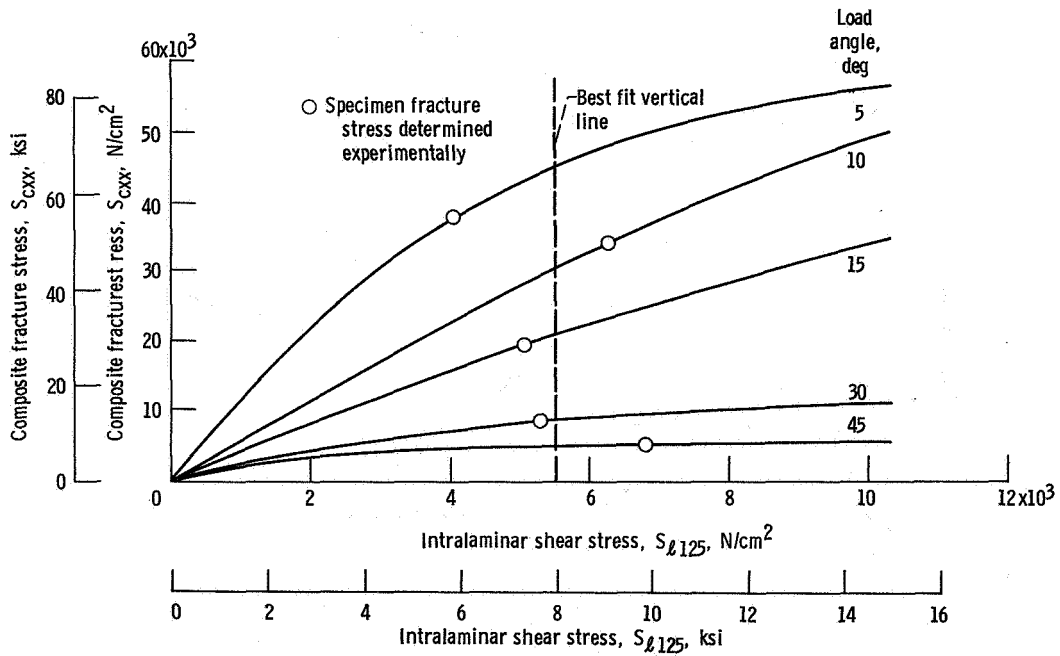
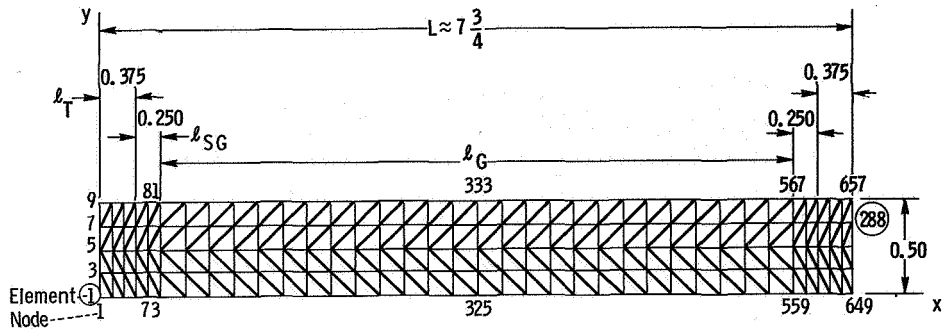


Figure 8. - Calculated fracture stresses for various assumed intralaminar shear stresses for Mod I/E unidirectional composite.



- L Length of test section  $l_G$  plus tapered portion of end tabs
- $l_T$  Length of tapered portion of Micarta end tabs
- $l_{SG}$  Section just beyond tapered portion of end tabs and site of top gages

Figure 9. - Grid for finite-element analysis of Mod I/E specimens. (Top gages located at nodes 74 and 77; midpoint gages located at nodes 326, 329, and 332. All dimensions shown are relative.)

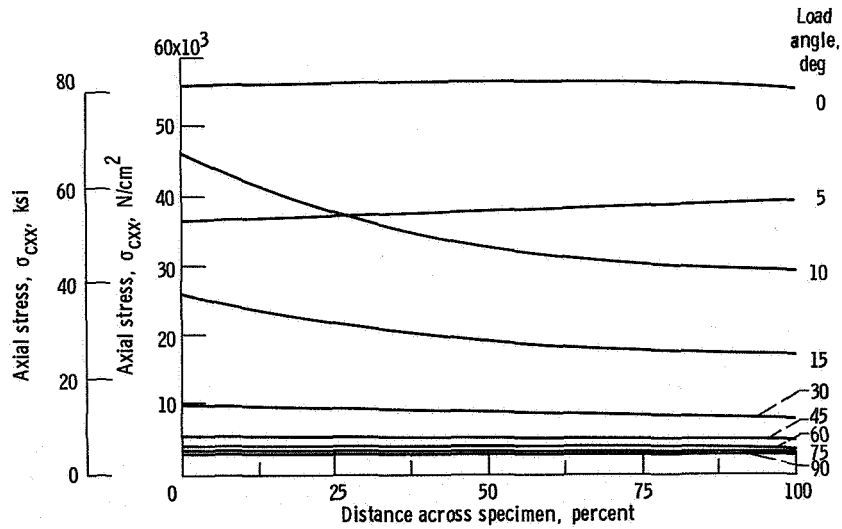


Figure 10. - Axial stress variation at tab ends for Mod I/E specimens for several load angles (finite-element analysis).

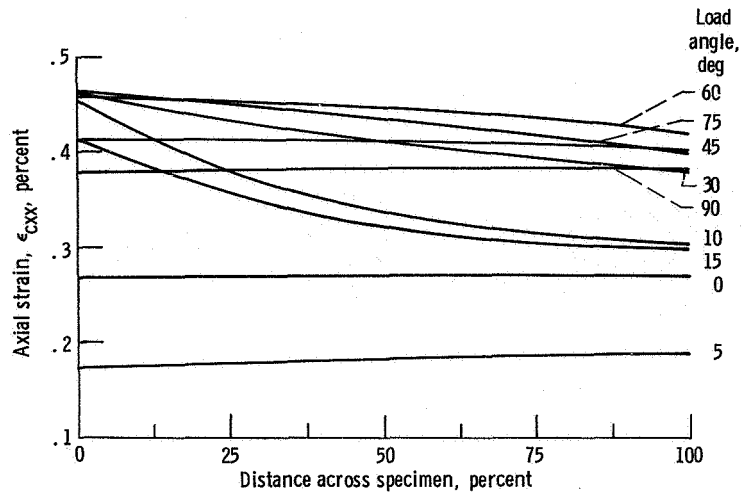


Figure 11. - Axial strain variation at tab ends for Mod I/E specimens for several load angles (finite-element analysis).

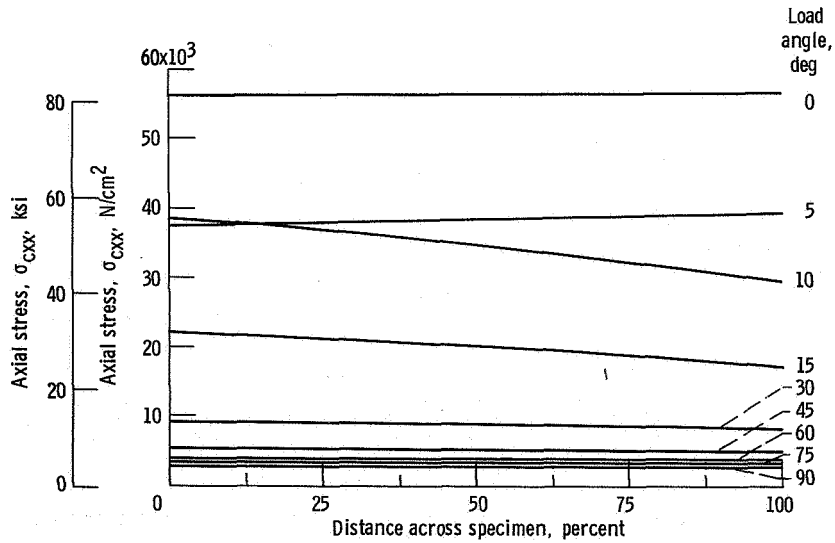


Figure 12. - Axial stress variation at midlengths for Mod I/E specimens for several load angles (finite-element analysis).

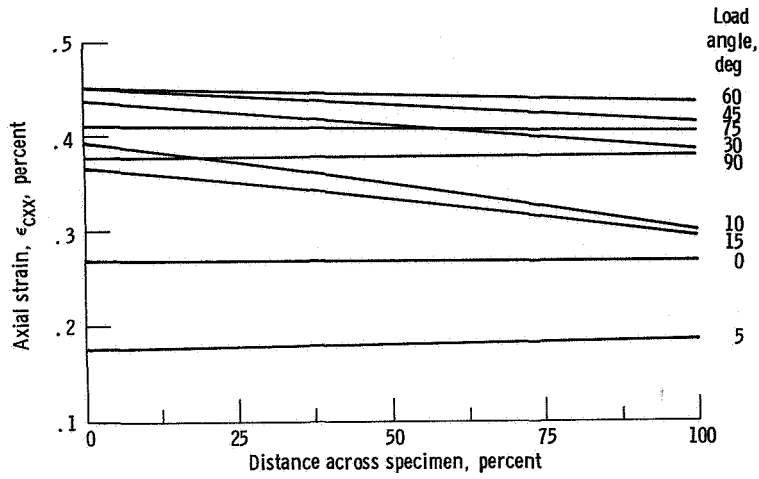


Figure 13. - Axial strain variation at midlengths for Mod I/E specimens for several load angles (finite-element analysis).

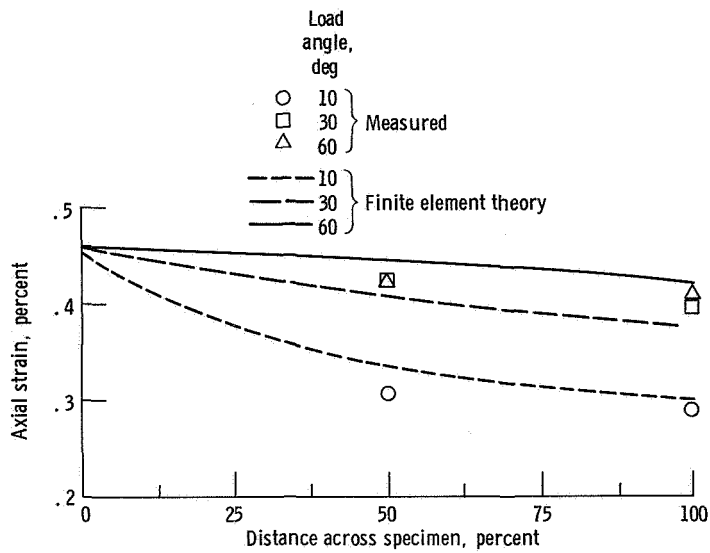


Figure 14. - Comparison at fracture load of predicted and measured axial strains near end tabs for off-axis specimens from Mod I/E.

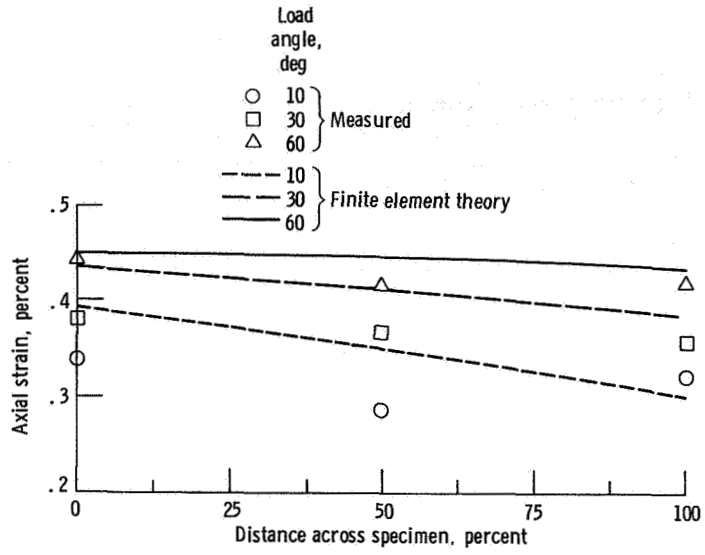


Figure 15. - Comparison at fracture load of predicted and measured axial strains at midlength of off-axis specimens from Mod I/E.

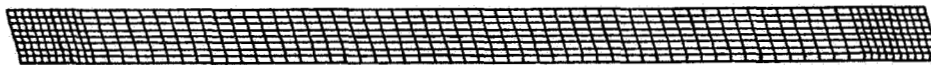
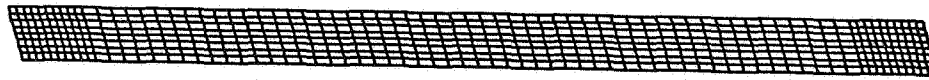
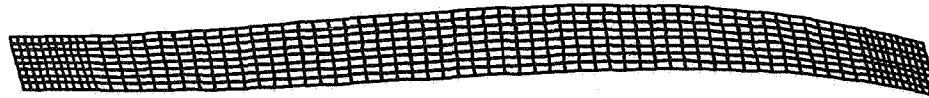


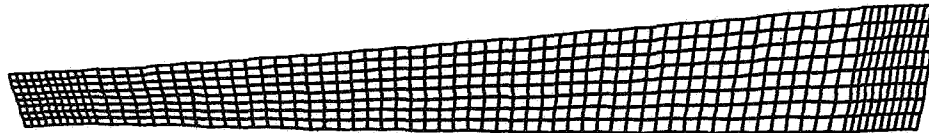
Figure 16. - NASTRAN model of off-axis specimen (657 nodes; 576 CQUAD2 elements).



(a) Undeformed.

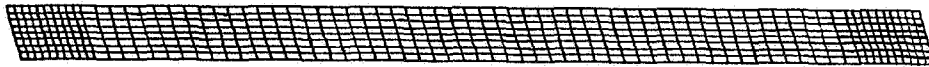


(b) Out-of-plane bending moment (11.30 N·m (100 in·lb)); maximum deflection, 4.25 cm (1.672 in.)).

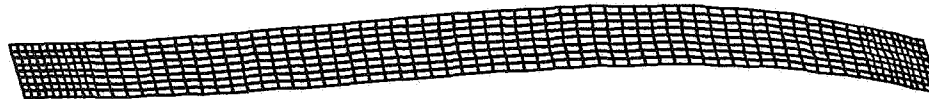


(c) Out-of-plane twisting moment (11.30 N·m (100 in·lb)); maximum deflection, 9.29 cm (3.658 in.)).

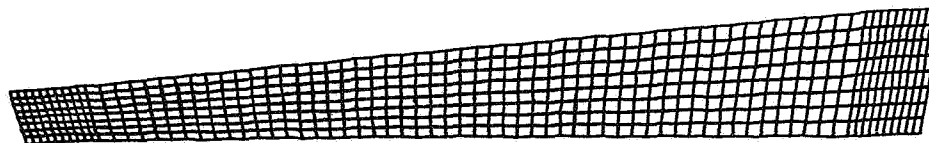
Figure 17. - NASTRAN plots of the 10<sup>0</sup> off-axis specimen showing deformed shapes due to out-of-plane eccentricities (Mod I/E).



(a) Undeformed.



(b) Out-of-plane bending moment (11.30 N·m (100 in·lb)); maximum deflection, 16.35 cm (6.437 in.)).



(c) Out-of-plane twisting moment (11.30 N·m (100 in·lb)); maximum deflection, 5.72 cm (2.250 in.)).

Figure 18. - NASTRAN plots of the 30<sup>0</sup> off-axis specimen showing deformed shapes due to out-of-plane eccentricities (Mod I/E).

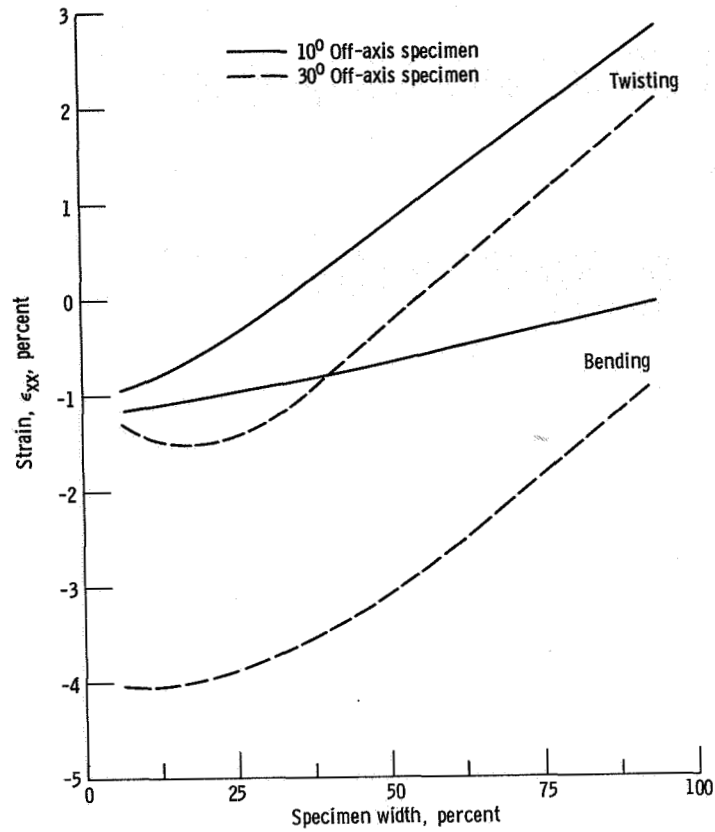


Figure 19. - Out-of-plane bending and twisting effects on axial strain near grips of  $10^{\circ}$  and  $30^{\circ}$  off-axis specimens from Mod I/E composites (11.3 N·m (100 in·lb) moments).

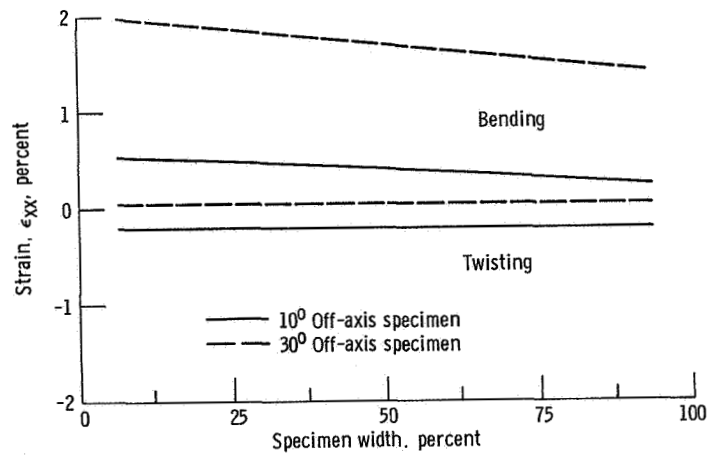


Figure 20. - Out-of-plane bending and twisting effects on axial strain at midlength of  $10^{\circ}$  and  $30^{\circ}$  off-axis specimens from Mod I/E composite (11.3 N·m (100-in·lb) moments).

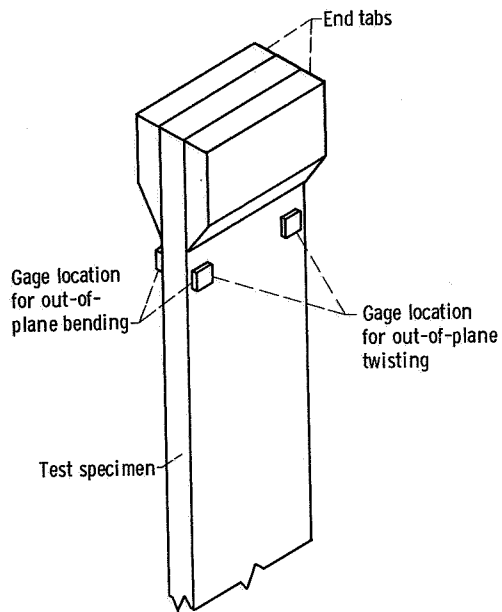


Figure 21. - Schematic depicting instrumentation to detect out-of-plane eccentricities during testing of off-axis fiber composites.

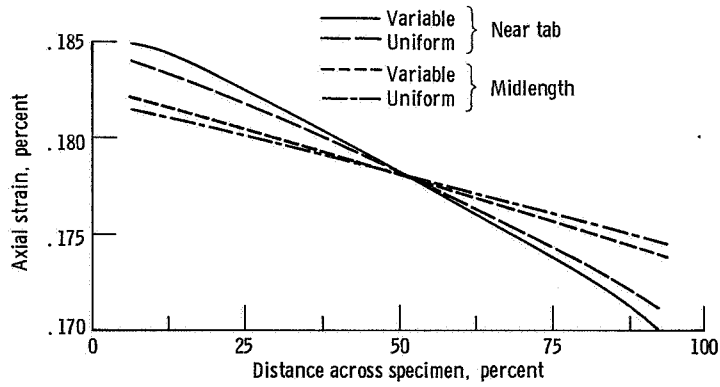


Figure 22. - Comparison of finite-element analysis results for 5° off-axis specimen (Mod I/E) showing effects of specimen thickness variation.

1. Report No. <b>TP-1082</b>		2. Government Accession No.		3. Recipient's Catalog No.	
4. Title and Subtitle <b>MECHANICAL BEHAVIOR AND FRACTURE CHARACTERISTICS OF OFF-AXIS FIBER COMPOSITES II - THEORY AND COMPARISONS</b>				5. Report Date <b>January 1978</b>	
				6. Performing Organization Code	
7. Author(s) <b>by Christos C. Chamis and John H. Sinclair</b>				8. Performing Organization Report No. <b>E-9269</b>	
9. Performing Organization Name and Address <b>National Aeronautics and Space Administration Lewis Research Center Cleveland, Ohio 44135</b>				10. Work Unit No. <b>506-17</b>	
				11. Contract or Grant No.	
12. Sponsoring Agency Name and Address <b>National Aeronautics and Space Administration Washington, D.C. 20546</b>				13. Type of Report and Period Covered <b>Technical Paper</b>	
				14. Sponsoring Agency Code	
15. Supplementary Notes					
16. Abstract <p>The mechanical behavior and stresses inducing fracture modes of unidirectional high-modulus graphite-fiber/epoxy composites subjected to off-axis tensile loads were investigated theoretically. The results are compared with experimental data. The investigation included the use of composite mechanics, combined-stress failure criteria, and finite-element stress analysis. The results led to the formulation of criteria and convenient plotting procedures for identifying, characterizing, and quantifying these fracture modes.</p>					
17. Key Words (Suggested by Author(s)) <b>Fiber composites; Off-axis tensile loading; High-modulus; Graphite fiber; Epoxy; Theoretical; Comparisons; Fracture modes; Criteria; Composite mechanics; Combined-stress fracture; Finite element</b>			18. Distribution Statement <b>Unclassified - unlimited STAR Category 24</b>		
19. Security Classif. (of this report) <b>Unclassified</b>		20. Security Classif. (of this page) <b>Unclassified</b>		21. No. of Pages <b>28</b>	22. Price* <b>A03</b>

\* For sale by the National Technical Information Service, Springfield, Virginia 22161